Moment transfer and influence of transverse beams in interior waffle flat plate–column connections under lateral loading

A. Benavent-Climent *, J. Donaire-Ávila

Department of Structural Mechanics, University of Granada, Granada 18071, Spain

A B S T R A C T

This paper addresses two aspects of the behavior of interior reinforced concrete waffle flat plate–column connections under lateral loads: the share of the unbalanced moment between flexure and excentric shear, and the effect of the transverse beams. A non-linear finite element model (benchmark model) was developed and calibrated with the results of quasi-static cyclic tests conducted on a 3/5 scale specimen. First, from this numerical model, the portion γ_v of the unbalanced moment transferred by the excentricity of shear about the centroid of the critical sections defined by Eurocode 2 (EC-2) and by ACI 318-11 was calculated and compared with the share-out prescribed by these codes. It is found that while the critical section of EC-2 is consistent with the γ_v provided by this code, in the case of ACI 318-11, the value assigned to γ_v is far below (about 50% smaller) the actual one obtained with the numerical simulations. Second, from the benchmark model, seven additional models were developed by varying the depth D of the transverse beam over the thickness h of the plate. It was found that the ductility of the connection and the effective width of the plate can respectively be increased up to 50% and 10% by raising D/h to 2 and 1.5.

Keywords:
Interior waffle flat plate–column connections
Transverse beams
Moment transfer
Seismic behavior
Non-linear finite element model

1. Introduction

Reinforced concrete (RC) waffle flat plate (WFP) structures have been commonly employed in moderate seismic zones such as the Mediterranean area for residential and administrative buildings. Important advantages of this structural system stem from its comparatively quick and easy cast (with respect to formworks), which implies cost reductions. However, WFP structures present important drawbacks, such as their low stiffness and limited ductility, when used in seismic areas. In the Mediterranean area, WFP structures are commonly used as the main lateral resisting system for low-to-medium height buildings. Such is the case of Spain, where the current seismic code NCSE-02 [1] classifies the WFP structure as "low ductility" and limits the behavior factor that reduces the design elastic response spectrum to 2.

One important issue when designing WFP systems under lateral loads is how to distribute the unbalanced moment caused by the lateral loading in the connection, between flexure and excentric shear mechanisms. This matter has been addressed by Eurocode 2 (EC-2) [2] and ACI 318-11 [3], providing different results depending on which one is applied. Codes and past research focuses on this problem for solid slabs [4,5], assuming that WFPs and solid slabs behave in the same manner under load. The fact is, however that differences exist [6], including the increased ratio of flexural to torsional rigidity in a waffle flat-plate, which might result in a substantial reduction in the load transmitted by torsion.

Commonly, deep transverse beams are added to the slab of WFP systems, as shown in Fig. 1, when the length of the bay is important (i.e. larger than about 10 m) to increase the flexure and torsional rigidity. The rigidity of the transverse beams can influence the width of the slab considered effective in transferring the portion of the unbalanced moment assigned to the flexure mechanism. The rigidity of these transverse beams can also affect the ductility of the connection, which is an indicator of its energy dissipation capacity.

This study presents a numerical investigation aimed at clarifying the distribution of the unbalanced moment between flexure and excentric shear mechanisms, and evaluating the influence of the transverse beams in interior connections of WFP systems. In contrast to previous research that used elastic models [7,8] in this study non-linear finite element models calibrated with experimental results are employed.

2. Development of benchmark numerical model and validation with test results

2.1. Experimental background

A six story prototype RC structure consisting of WFPs supported on columns was designed. The columns were arranged in plan

* Corresponding author. Tel./fax: +34 958 246109.
E-mail address: benavent@ugr.es (A. Benavent-Climent).

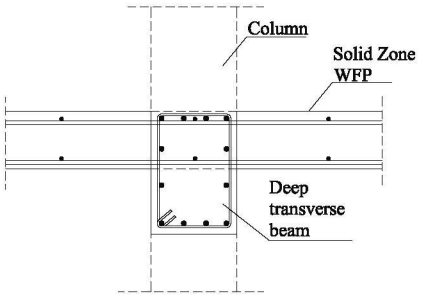

Fig. 1. Cross section of a WFP system with deep transverse beams.

forming a regular layout with three bays in two orthogonal directions. The structure was assumed to be located in the most earthquake-prone region of Spain (Granada). The WFP consisted of a 0.7×0.7 m grid of ribs and its total thickness was 0.3 m. A square solid zone with a total width of 2.8 m was left around the columns, provided with shear reinforcement consisting of closed-hoop stirrups. The design gravity loading on each floor consisted of the plate self weight plus 1 kN/m^2 superimposed dead load and 3 kN/m^2 live load. The design lateral earthquake loads consisted of an inverted triangular distribution. The base shear normalized by the total building weight was 0.11. The WFP structure was designed using the equivalent frame method. Concrete was specified for a 28-day compressive strength of 17.5 MPa, and the design yield stress of reinforcement was 400 MPa.

From the prototype structure, one interior WFP–column connection was selected from the third story of the building. The width of the selected portion of the plate, measured perpendicularly to the direction of loading, coincided with the width of a column strip as defined by ACI 318-11. It was also equal to the width of the solid zone of the plate around the column. The modeling and boundary conditions of the subassemblage were based on the assumption that points of inflection in the prototype structure under lateral loading are located at mid-span and mid-story height. From the interior WFP–column connection selected, the corresponding test model was derived by applying a scaling factor of 3/5 for geometry. It is shown in Fig. 2. The test model was built in the laboratory. The average yield stress of the steel used for the reinforcement (deformed steel bars) was 405 MPa, and the average compressive strength of the concrete 19.4 MPa. The test specimen was mounted in the set-up shown in Fig. 3. It was subjected to four vertical forces (10 kN each, applied through bags of sand as shown in Fig. 4) that remained constant during the tests, and cycles of imposed lateral displacement with increasing amplitude at the upper end of the column, following the history shown in Fig. 5. The loading history consisted of three cycles with increasing amplitude, and three sets of cycles (each one containing three cycles of constant amplitude) that are identified in Fig. 5 as sets A, B and C. The experimental load–interstory drift index *Q–IDI* curve obtained from the tests is shown with thin lines in Fig. 6, where the interstory drift index *IDI* is defined as the ratio between the displacement at the top of the column and its length measured between the pin ends (Fig. 3). A more detailed description of the tests can be found in [9].

2.2. Benchmark numerical model

2.2.1. Finite element model (FEM) of the specimen

For the purposes of the present study, a finite element model was developed [19] to represent the WFP–column connection tested in the aforementioned experimental investigation. Columns and ribs were idealized using frame elements (FE) of three nodes with fiber models (2 Gauss point scheme). The solid zone of the

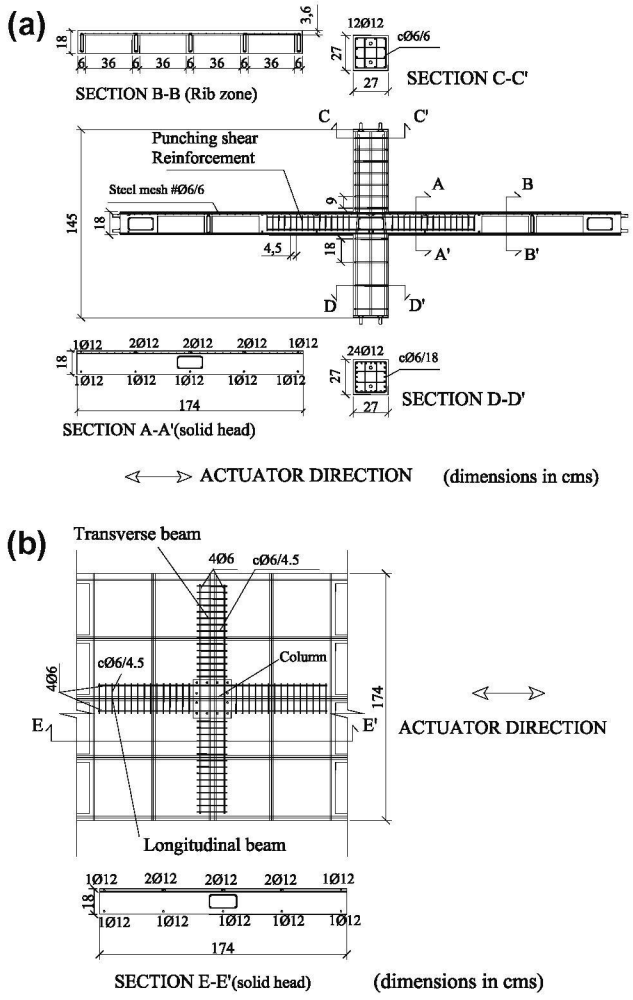

Fig. 2. Geometry and reinforcement of the specimen: (a) elevation and (b) plan.

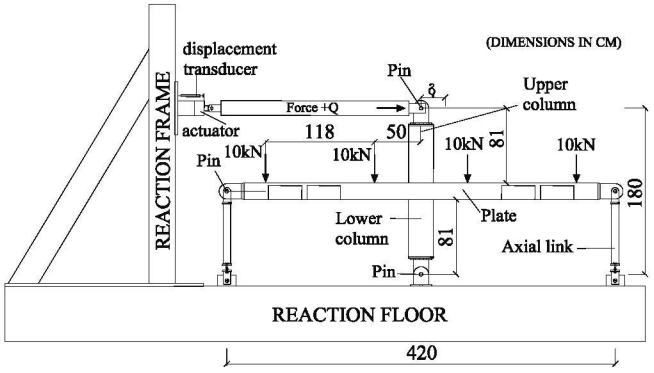

Fig. 3. Test set-up.

slab around the columns, which included the embedded punching shear reinforcement, was modeled with four nodes of layer-shell elements (LE) (2×2 Gauss point scheme). The layered approach was adopted for the LE, according to which the shell is divided into several layers along its depth. Each layer of the shell element can have a different thickness. A layer is classified as a reinforced concrete layer if it contains reinforcement; otherwise it is defined as an un-reinforced layer. In the reinforced concrete layers, reinforcement is uniformly distributed over the layer depth, and by applying constitutive equations the total stresses can be calculated as the summation of concrete and reinforcement stresses. Normal

Fig. 4. Set-up of the experiments.

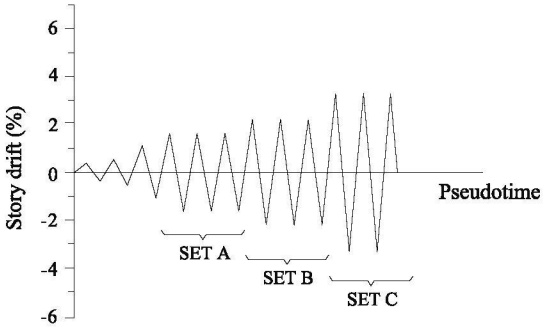

Fig. 5. History of lateral cyclic forced displacements.

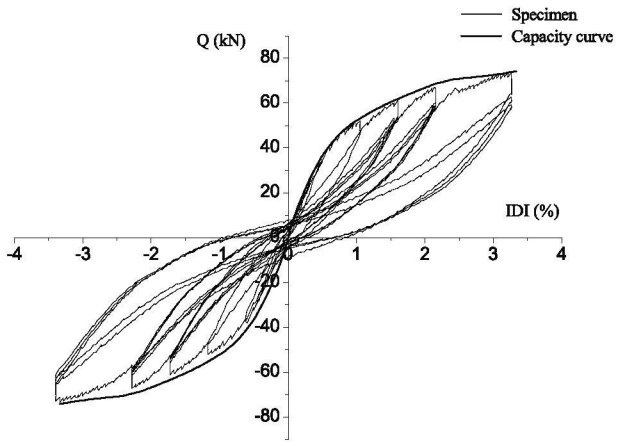

Fig. 6. Load–displacement *Q–IDI* curve obtained from the tests and capacity curve predicted numerically from a pushover analysis.

σ_y and shear τ_{xz}, τ_{yz} stresses are computed at the mid-depth of each layer and are assumed to be constant over the thickness of the layer. This provides a piecewise approximation of the stress distribution throughout the thickness of the shell element.

Fig. 7 shows the numerical model, referred to hereafter as the benchmark model, with the boundary conditions applied during the tests. A more detailed description of the numerical model can be found in [10].

2.2.2. Constitutive models for concrete and steel reinforcement

The non-linear mechanics of RC proposed by Maekawa et al. [11] were adopted in formulating the constitutive relationships

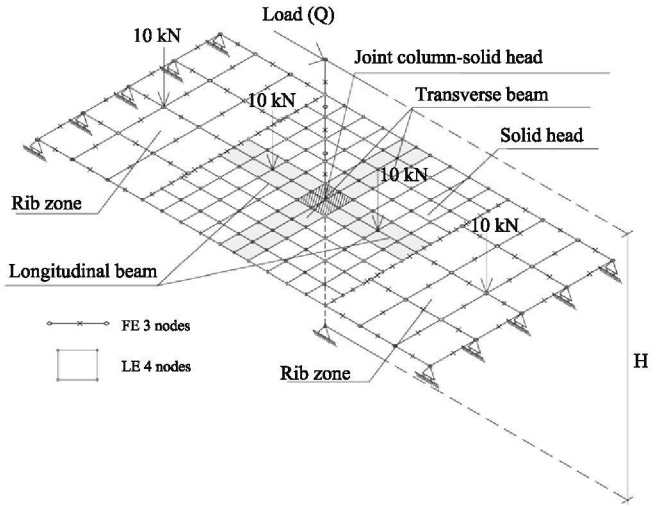

Fig. 7. Benchmark numerical model (FE: frame element; LE: layer element).

Table 1
Parameters used for modeling concrete before cracking and steel reinforcement.

	Young modulus (N/mm²)	Poisson coeff.	Yield strength (N/mm²)	Ultimate strength (N/mm²)
Concrete	$E_{c0} = 27.000$	$\upsilon_c = 0.167$	$f_{cy} = 19$	–
Steel	$E_{y0} = 200.000$	$\upsilon_s = 0.30$	$f_{sy} = 400$	$f_{su} = 428$

of the materials. This theory is based on a complete analysis of the different stress–strain states of RC before and after cracking. Before cracking, the elasto-plastic fracture model (EPF) [11] is applied for the concrete, and the required parameters to define the model are the initial stiffness (E_{c0}), compression strength (f_{cy}) and Poisson coefficient (υ_c) of the concrete. The behavior of the steel reinforcement is determined by the constitutive law of bare bars, and the controlling parameters are the initial stiffness (E_{y0}), yield strength (f_{sy}), ultimate strength (f_{su}) and Poisson coefficient (υ_s). Table 1 shows the values for these parameters as adopted in this study. Once cracks appear on the concrete, the smeared crack model (SCM) [12] is used.

2.2.3. Distribution of the unbalanced moment

For a given critical section such as defined by the perimeter shown in Fig. 8, the numerical model provides the normal σ_y and shear τ_{yz}, τ_{xz} stress distribution over the shell thickness. The internal bending moments M_f^+, M_f^- transferred by flexure across the two opposite cross sections of the critical perimeter that are perpendicular to the loading direction (sides AB and CD in Fig. 8) are computed from the internal normal stresses σ_y acting on every layer over the thickness of the cross section. The integration of the normal stresses acting on side AB of the critical section multiplied by the distance z to the mid-thickness of the cross section provides M_f^+, while the corresponding integration with the normal stresses acting on side CD of the critical section provides M_f^-. The moment transferred by bending M_f is calculated by $M_f = |M_f^+| + |M_f^-|$. The moment transferred by eccentricity of shear M_v is calculated by integrating the moment induced about the centroidal axis a–a' of the critical section by the shear stresses τ_{yx} and τ_{xz} (Fig. 8) acting on every layer over the thickness of the cross sections and along the perimeter of the critical section (sides AB, BC, AD and CD in Fig. 8). The unbalanced moment M_u is calculated in each step of the sequence of loading by multiplying the horizontal loading force

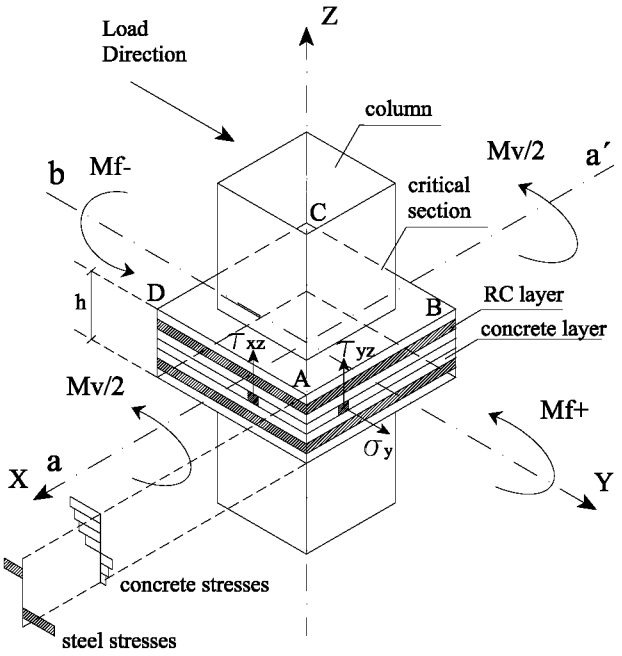

Fig. 8. Stresses in layer elements.

Q applied at each column end by the distance H (see Fig. 7). For a given critical perimeter and in each step of the loading history, the analysis results always verify that $M_u = M_f + M_v$.

2.3. Validation of the benchmark numerical model

First, the numerical model was subjected to a push-over analysis by applying a monotonically increasing forced displacement δ at the upper end of the column until flexural failure on the plate occurred. Failure was assumed to occur when the first concrete layer of the shell element (see Section 2.2.1) subjected to compression attained its maximum compression strain while the longitudinal reinforcement located on the tension side was yielding. Flexural failure was assumed to occur when the aforementioned concrete compressive strain was in the range 0.25–0.35%. The measured reaction force is referred to as Q. The corresponding capacity curve, *Q–IDI*, was obtained as shown with bold lines in Fig. 6. As seen in the figure, the benchmark numerical model provides a good approximation of the envelope of the cyclic loops obtained from the tests.

A second analysis was conducted to validate the benchmark numerical model by subjecting it to the history of cyclic forced lateral displacements applied to the specimen during the tests, until the onset of severe strength degradation. Similarly to the numerical model, the onset of strength degradation on the test specimen was due to the flexural failure of the plate; punching shear failure was not observed. The predicted hysteretic curves are compared with the test results in Fig. 9, for the single cycle of 1.1% drift, and for each set of cycles A, B and C. As seen, there is a reasonable fit between predicted and tested hysteretic loops. The layered approach applied in this study to model the connection and the theories involved (elasto plastic fracture model, smeared crack theory) are well established in the literature [11] and have been validated

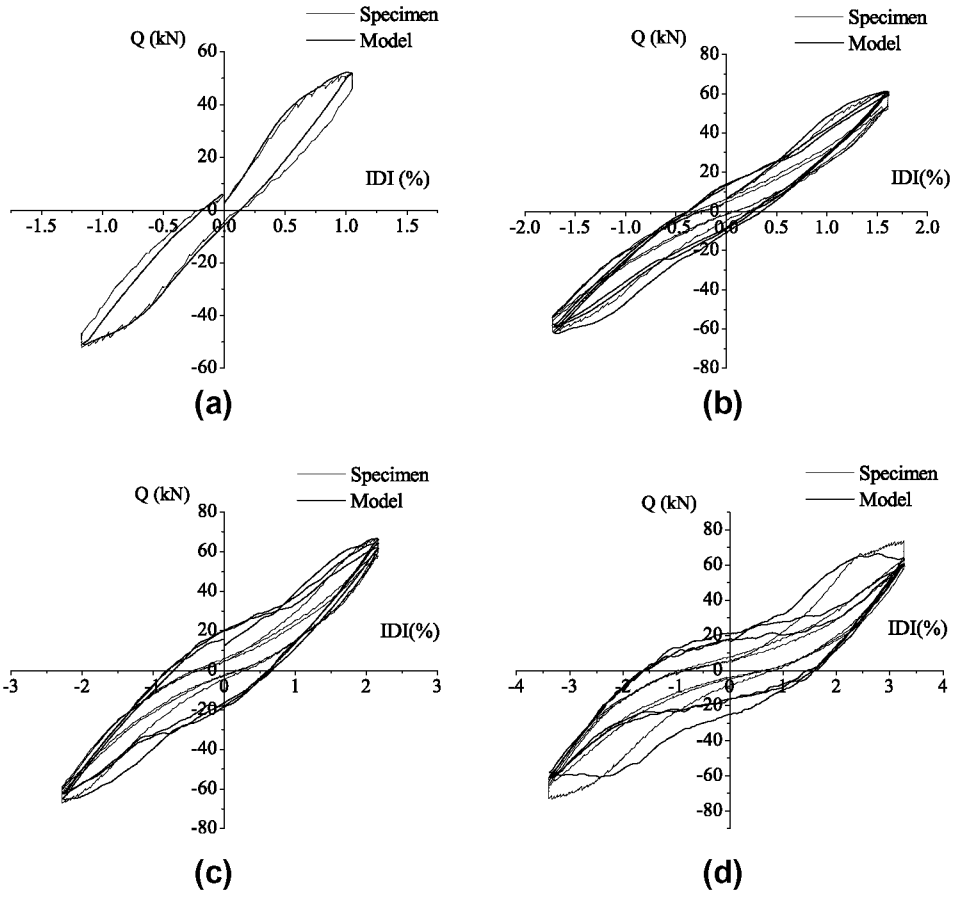

Fig. 9. Comparison between the hysteretic loops predicted with the numerical model and test results: (a) single cycle of 1.1% drift; (b) set of cycles A; (c) set of cycles B; (d) set of cycles C.

previously on slab models by comparison with the results of a large number of laboratory tests [13,14].

3. Development of numerical models with transverse beams of different depths

It is common to design WFP structures with large spans (8–15 m) that are different in both directions in plan. It is also usual to design structures with a larger number of bays in one direction than in the perpendicular one. These situations can lead to different depths of transverse and longitudinal beams. To investigate the influence of the transverse beams several numerical models were developed from the benchmark model by increasing the depth D of the transverse beam. Besides the benchmark model whose depth is D = 0.18 m (referred to as model D18 hereafter), seven new numerical models were developed for D = 0.21, 0.24, 0.27, 0.30, 0.36, 0.42 and 0.48 m [19]. They are denoted as models D21, D24, D27, D30, D36, D42 and D48, respectively. Taking into account that the benchmark numerical model was derived using a scaling factor of 3/5 for geometry, the depth of the transverse beams in the full scale WFP–column connection ranges from 0.3 m to 0.8 m, which are realistic values representative of actual structures. In the benchmark numerical model the transverse beam is embedded in the thickness of the solid head and it is reinforced with four longitudinal bars of 6 mm diameter (Ø6), and closed Ø6 stirrups spaced 45 mm. The torsion reinforcement of the transverse deep beams consisted on longitudinal bars and closed stirrups as transverse reinforcement and it was designed to sustain the torsion induced by the lateral load, according to the Spanish code EHE-08 [15]. The amount of reinforcement used to prevent torsional failure on the transverse beam is shown in Table 2, where c_1 is the dimension of the column parallel to the direction of loading, M_{TD} is the torsional moment capacity of the transverse beam and Q_u is the maximum lateral force reached by the connection that corresponds with the maximum unbalanced moment M_{umax}.

Table 2
Reinforcement and capacity of the deep transverse beams.

Model	c_1 (mm)	D (mm)	Longitudinal rebar (perimeter section)	Stirrup (s/mm)	M_{TD} (kN m)	Q_u (kN)	M_{umax} (kN m)
D21	270	210	14Ø12	1Ø8@15	67.88	74.17	133.51
D24	270	240	14Ø12	1Ø8@15	73.41	77.38	139.28
D27	270	270	14Ø12	1Ø8@20	78.11	79.25	142.65
D30	270	300	14Ø12	1Ø8@20	82.12	79.73	143.51
D36	270	360	16Ø10	1Ø8@20	73.48	81.37	146.47
D42	270	420	16Ø10	1Ø8@20	77.35	80.55	145.00
D48	270	480	16Ø10	1Ø8@20	80.23	80.99	145.78

The transverse beams were modeled with rectangular layer-shell elements featuring four nodes as shown in Fig. 10.

Each layer-shell element uses 10 layers to model the cross section depth of the transverse beam. The column was modeled with 3-node frame elements. The joint between the column, the solid head of the WFP and the transverse beam was considered rigid. To this end, rigid elements were inserted connecting all nodes of the joint, as shown in Fig. 10 with bold lines. Similarly to the assumptions made in the benchmark model, non-linear multilinear models for the steel and non-linear continuum fracture model for concrete were used as constitutive models of the materials. A detailed description of the numerical model used for representing the connections can be found in Ref. [10].

4. Distribution of unbalanced moment between flexure and excentric shear

The unbalanced moment M_u acting on the connection due to the lateral actions is transferred from the column to the solid zone of the plate through two types of mechanisms: flexure and eccentric shear. The former involves normal stresses on the cross section of the plate, whereas the later induces shear stresses in the critical cross section around the column. According to code ACI 318-11 [3], the portion of the unbalanced moment transferred by flexure, $M_f = \gamma_f M_u$, is determined by a coefficient γ_f defined as follows:

$$\gamma_f = \frac{1}{1 + (2/3)\cdot\sqrt{c_1/c_2}} \tag{1}$$

For square columns γ_f = 0.60. ACI 318-11 [3] code assumes that M_f is resisted by a strip of slab having width $b_{eff} = c_2 + 3h$. The remaining part of the unbalanced moment, $M_v = (1-\gamma_f)M_u$, shall be considered transferred by eccentricity of shear about the centroid of a critical section whose perimeter is defined in different ways depending upon the code. For ACI 318-11 the perimeter of the critical section is defined at a distance $d/2$, where d is the

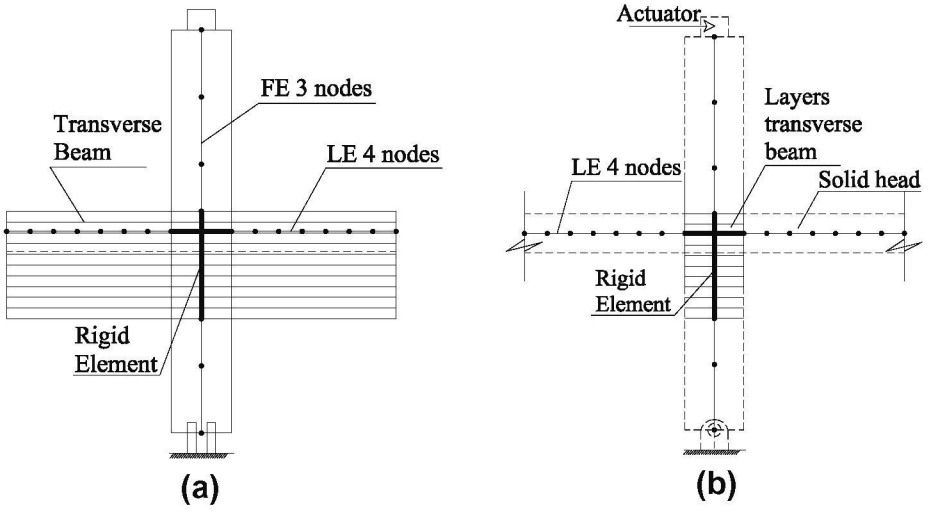

Fig. 10. FEMs of the WFP–column connections with transverse beams (FE: frame elements; LE: layer-shell elements): (a) cross section perpendicular to the loading direction and (b) cross section in the loading direction.

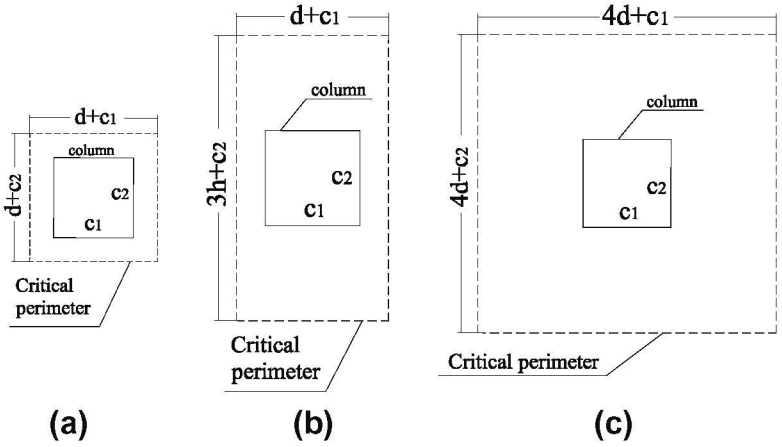

Fig. 11. Perimeter of the critical section according to: (a) ACI 318-11; (b) ACI 318-62 and (c) Eurocode 2.

effective depth, measured from the faces of the column as shown in Fig. 11a. It is worth noting that the dimension of this perimeter perpendicular to the direction of lateral loading, $(d + c_2)$, does not coincide with the width $b_{eff} = c_2 + 3h$ adopted by ACI 318-11 to transfer M_f. This issue has been addressed in past studies [4]. Apparently more consistent, however, is the approach used by ACI 318-62 code [16]; it assumes a perimeter for the critical section whose size perpendicular to the loading direction coincides with the effective width $b_{eff} = c_2 + 3h$ that transfers flexure, as shown in Fig. 11b. In turn, EC-2 [2] defines the perimeter of the critical section at a distance $2d$ from the column face as shown Fig. 11c. In contrast to ACI 318-11, for square columns the fraction of unbalanced moment transferred by flexure according to EC-2 is $\gamma_f = 0.40$.

In this section, the distribution of M_u between the flexure and the excentric shear mechanisms in the benchmark numerical model is analyzed and compared with the provisions of codes ACI 318-11, ACI 318-62 and EC-2. To this end, the numerical results of the pushover analysis conducted with the benchmark model in Section 2.3 are used. The unbalanced moment attained by the benchmark model when it reached the maximum lateral load Q_u was $M_u = 131.2$ kN m, which includes the gravity load moments.

As noted, according to ACI 318-11, the portion of M_u transferred by the flexure mechanism $\gamma_f M_u$ is resisted at column face by a section of width $b_{eff} = c_2 + 3h$. The total bending moment M_f transferred at the two opposite column faces in the benchmark numerical model (Fig. 11b) when the unbalanced moment attained its maximum value was $M_f = M_f^- + M_f^+ = 49.0 + 25.0 = 74.0$ kN m, and it represents the flexural strengths of the sections. This value of $M_f = 74.0$ kN m represents a fraction of 0.56 (=74.0/131.2) of the applied unbalanced moment M_u. This fraction of M_u transferred by flexure in the numerical model is very close to the lower bound of the range of values prescribed by ACI 318-11 for γ_f, which is between 0.60 and $1.25 \cdot 0.60 = 0.75$. Section 13.5.3.3 of ACI 318-11 permits this increase of γ_f up to 0.75 when two conditions related to the value of the gravity shear force and the amount of reinforcement are fulfilled; such conditions are satisfied by the interior connection used as the benchmark model in this study.

Code ACI 318-11 considers that the remaining portion of the unbalanced moment M_u, i.e. 131.2–74.0 = 57.2 kN m, is transferred by excentricity of shear about the centroid of the critical section defined in Fig. 11a. The moment transferred by excentricity of shear about the centroid of this critical section in the benchmark model was calculated giving $M_v = 90.30$ kN m, which represents a portion of unbalanced moment of 0.69 (=90.3/131.2). This value 0.69 is similar to that obtained in previous studies [7,8] from numerical simulations with elastic models (from 0.55 to 0.66), but clearly larger and outside the range prescribed by ACI 318-11 code, which is between 0.40 (=1.0–0.6) and 0.25 (=1.0–0.75). The differences between elastic and inelastic response in this type of connections have been addressed in previous studies [17]. What is worth emphasizing here is that, according to this results, checking the shear capacity of the connection by estimating the shear stress at the critical section defined by ACI 318-11 with values of γ_v between 0.40 and 0.25 is not realistic and can lead to a design on the unsafe side.

It is worth noting that $M_f = 74.0$ kN and $M_v = 90.30$ kN m are not calculated in the same critical section, and this is the reason why the sum does not give $M_u = 131.2$ kN m. As indicated above, $M_f = 74.0$ kN was calculated for a width of $c_2 + 3h$ while $M_v = 90.30$ kN m was estimated for the critical section shown in Fig. 11a, whose dimension perpendicular to the loading direction is not $c_2 + 3h$ but $d + c_2$. The value of M_v obtained with the numerical model in the critical perimeter shown in Fig. 11b (whose width perpendicular to the loading direction $c_2 + 3h$ coincided with that used for calculating $M_f = 74.0$ kN) was 57.2 kN m, and therefore 74.0 + 57.20 = 131.2 kN m.

In contrast to ACI 318-11, in code ACI 318-62 the effective width of slab assumed to transfer M_f coincided with the dimension of the perimeter of the critical section perpendicular to the loading direction, as shown in Fig. 11b. The moment transferred by excentric shear through the critical section of Fig. 11b in the benchmark numerical model was calculated giving $M_v = 57.2$ kN m, which represents a portion of unbalanced moment of 0.44 (=57.2/131.2). The sum of the moment transferred by flexure along the width $b_{eff} = 3h + c_2$, i.e. 74.0 kN m, and by excentric shear through the critical section prescribed by the ACI 318-62 code gives the applied unbalanced moment $M_u = 131.20$ kN m, as expected.

The moment transferred by the excentricity of shear about the centroid of the critical section defined by EC-2 code (Fig. 11c) was also calculated in the benchmark numerical model giving $M_v = 87.9$ kN m. This value of M_v represents a portion of unbalanced moment of 0.67 (=87.9/131.2), which is close to the γ_v implicit in the EC-2 code, i.e. $\gamma_v = 0.60$ (=1.0–0.4).

Table 3 summarizes the portions of unbalanced moment considered to be transferred by excentricity of shear by ACI 318-11 and by EC-2, $\gamma_{v,\mathrm{CODE}}$, and the portions calculated with the corresponding critical sections using the benchmark numerical model, $\gamma_{v,\mathrm{MODEL}}$. It follows from Table 3 that the critical section defined by EC-2 is consistent with the value γ_v that this code prescribes to check the shear capacity of the connection. In contrast, ACI 318-11 gives a value for γ_v that represents the 58% of the shear

Table 3
Comparison between γ_v prescribed by codes and numerical results.

Code	ACI 318-11	EC-2	ACI-1962
$\gamma_{v,CODE}$	0.40	0.60	–
$\gamma_{v,MODEL}$	0.69	0.67	0.44
$\gamma_{v,CODE}/\gamma_{v,MODEL}$	0.58	0.90	–

stress acting at the critical section defined by the same code according to the numerical model. ACI 318-62 did not provide a value for γ_v, but Table 3 shows that the shear stress at the critical section defined by ACI 318-62 can be accurately estimated with the upper bound value for γ_v prescribed by ACI 318-11 (i.e. $\gamma_v = 0.40$). Non-linear finite element analyses by Gayed and Ghali [18] showed that the values of γ_v for interior and edge column–slab connections permitted by ACI 318-11 are too low.

5. Influence of transverse beams

Along the lines of to the benchmark model D18, pushover analyses were conducted for the numerical models D21, D24, D27, D30, D36, D42 and D48. These models were subjected to a lateral force of monotonically increasing amplitude applied at the top end of the column, until flexural failure occurred. Flexural failure was assumed to occur when concrete attained its maximum compressive strain while the longitudinal reinforcement located on the tension side was yielding. Flexural failure occurred in the zone of negative bending moments (top longitudinal bars of the plate in tension). The capacity curves obtained from each pushover analysis are shown in Fig. 12. It can be seen in these curves that the depth D of the transverse beam does not affect the initial stiffness of the WFP–column connection. The depth D of the transverse beam scarcely affects the lateral strength. The lateral strength of the benchmark model D18 whose depth is $D = 0.18$ m is 72.89 kN, while the lateral strength of model D48 whose depth is $D = 0.48$ m is 80.99 kN. This represents an increase of 11%.

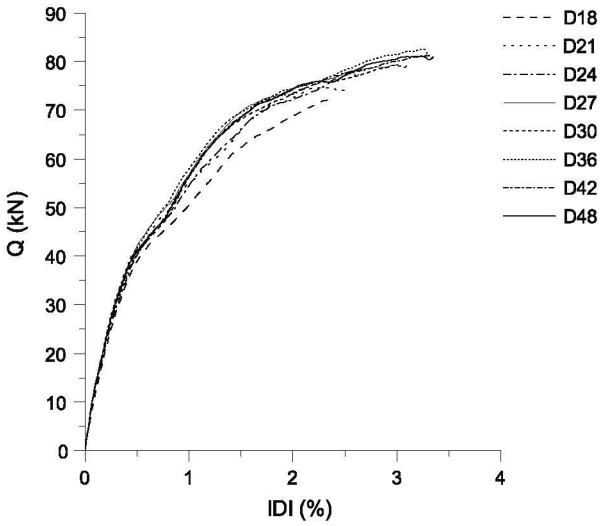

Fig. 12. Capacity curves of the numerical models with different depths for the transverse beams.

Fig. 13 illustrates the concrete cracking pattern at the upper surface of the plate for two of the numerical models investigated, D18 and D48. Fig. 13a corresponds to the model with shallow transverse beams (D18), and Fig. 13b to the model with deep transverse beams (D48).

The small segments in the figure indicate the direction of the horizontal cracks and their thickness is proportional to the crack width. The cracks on each LE are located at the Gauss points of each layer. Moreover, the crack width is calculated on each Gauss point through the value of the tension strain perpendicular to the crack direction [11]. In the model with shallow transverse beams (D18), inclined cracks tend to concentrate near the corner of the column. In contrast, in model D48 the level of diagonal cracking around the column is notably reduced. The greater depth of the transverse beam of model D48 in comparison to model D18 results in a reduction of the level of concrete cracking.

5.1. Influence of depth of the transverse beam on bending moment distribution

The distribution of bending moments along the cross section through which the numerical models failed in flexure was calculated, shown in Fig. 14. This distribution was calculated at the full cross section of the plate perpendicular to the loading direction and situated at $d/2$ from the column face, when flexural failure occurred under negative bending moments. This cross section intersects 10 LE, each with four nodes and a 2×2 Gauss point scheme. In turn, each LE was divided into 10 layers along its depth. A layer is classified as a reinforced concrete layer if it contains reinforcement; otherwise it is defined as an un-reinforced layer. In the reinforced concrete layers, reinforcement is uniformly distributed over

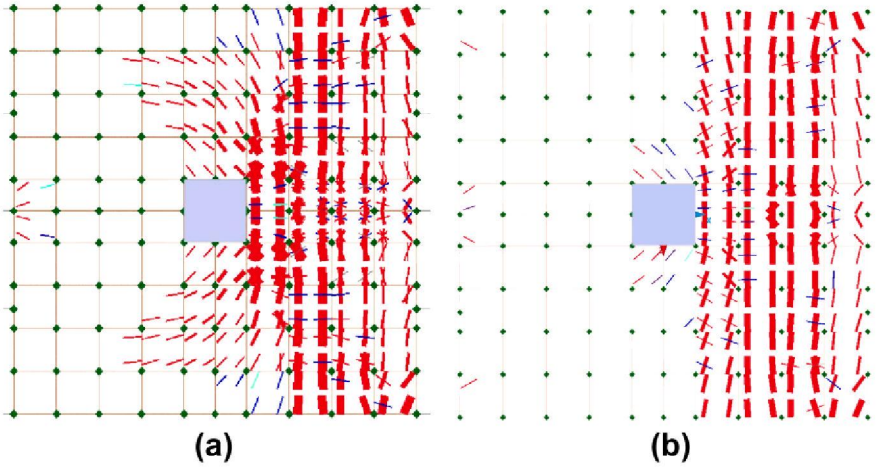

Fig. 13. Concrete cracking on the top surface of the plate in models: (a) D18 and (b) D48.

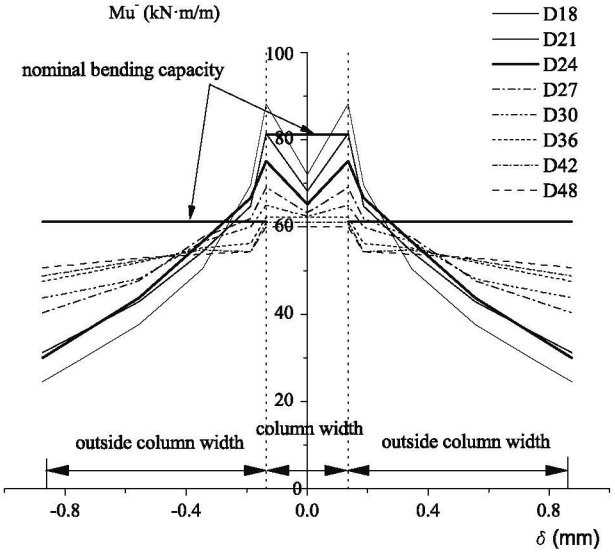

Fig. 14. Bending moment distribution.

the layer depth and by applying constitutive equations the total stresses can be calculated as the sum of concrete and reinforcement stresses. The program Engineer's Studio [19] used in this study computes the normal stress σ_{yi} at the mid-depth of the each layer and assumes that σ_{yi} is constant over the thickness t_i and over the length b of the layer. This provides a piecewise approximation of the stress distribution throughout the thickness of the shell element, as shown in Fig. 8. The internal bending moment M_f transferred by flexure across the cross section of each LE is computed from the internal normal stresses σ_{yi} acting on each layer i by $M_f = \sum z_i \sigma_{yi} t_i b$, where z_i is the distance from the mid-depth of the LE to the mid-depth of layer i, and the sum is extended to all the layers of the LE.

The solid horizontal line drawn at each side of the column represents the nominal bending capacity per unit length, 61.21 kN m/m, calculated with the following approximated equation:

$$M_f = A_s f_s d\left[1 - \frac{A_s f_s}{1.7 f_c' d}\right] \tag{2}$$

where A_s is the area of tension reinforcement per unit length outside the column width, f_s is the yield strength of the reinforcement, and f_c' is the concrete compressive strength. Eq. (2) was derived on the basis of the following assumptions: (i) the presence of compression reinforcement is disregarded; (ii) the tension in the steel per unit length, $A_s f_s$, is opposed by an equivalent unit width rectangular block of concrete stress equal to $0.85 f_c'$, whose depth is $\beta_1 c$. Here, β_1 is a constant that is taken equal to 0.85 following ACI-318-11, and c is the distance from the extreme compression surface to the neutral axis that is obtained by equating the resulting compression and tension forces.

In the strip of plate within the column width the amount of longitudinal reinforcement A_s is larger than outside the column width, because it includes the longitudinal rebars that sustain the stirrups used as punching shear reinforcement. Inside the column width, the nominal bending moment estimated with Eq. (2) gives 81.23 kN m/m.

When the depth of the transverse beam is low, and thus its torsional stiffness as well, stress concentration takes place near the column faces, resulting in bending moments larger than those calculated by Eq. (2). At increasing distances from the face of the column, the bending moment decreases sharply and is reduced to values roughly one half (at most) of the nominal bending moment calculated with Eq. (2). The bending moment distribution clearly flattens as the depth D of the transverse beam increases, but there is always a sudden increase of bending moment near the column face attributable to the presence of high shear stresses induced by the torsional moment applied by the transverse beam. Table 4 shows for each model, the total force Q_u applied to each model, the corresponding bending moment $M^-_{u,tot}$ on the full cross section of the plate located $d/2$ from the column face and subjected to negative bending, and the total unbalanced moment M_u.

5.2. Influence of the depth of the transverse beam on ductility

Each lateral load–interstory drift index curve, *Q–IDI*, obtained from the pushover analyses until flexural failure occurred (Fig. 12) was idealized by two segments as shown in Fig. 15. One segment passes through the origin and it is secant to the *Q–IDI* curve at $Q = 2/3 \cdot Q_{max}$. The other segment is horizontal and its ordinate coincides with the maximum lateral load attained by the connection. Similarly to previous studies [20], the intersection of the two segments is taken in this study as the yield interstory drift index, IDI_y. The ultimate interstory drift index attained by the interior connection when flexural failure occurred is referred to as IDI_u, and the ratio IDI_u/IDI_y is taken hereafter as the displacement ductility μ ($=IDI_u/IDI_y$).

Fig. 16 shows the variation of the ductility ratio μ with the depth D of the transverse beam expressed in terms of the thickness of the plate h. It can be observed that for $D/h < 2$ the ductility tends to increase with D/h. Beyond $D/h = 2$, increasing D/h does not improve μ. In contrast, Fig. 16 suggests that increasing D/h beyond some limit (approximately $D/h = 2$ for the connection investigated in this study) can reduce the ductility of the connection. The

Table 4
Values of Q_u, $M^-_{u,tot}$ and M_u for models with different transverse beam depths.

Model	Q_u (kN)	$M^-_{u,tot}$ (kN m)	M_u (kN m)
D18	72.89	85.40	131.20
D21	74.17	89.10	133.51
D24	77.38	90.20	139.28
D27	79.25	93.40	142.65
D30	79.73	93.50	143.51
D36	81.37	94.20	146.47
D42	80.55	93.90	145.00
D48	80.99	94.00	145.78

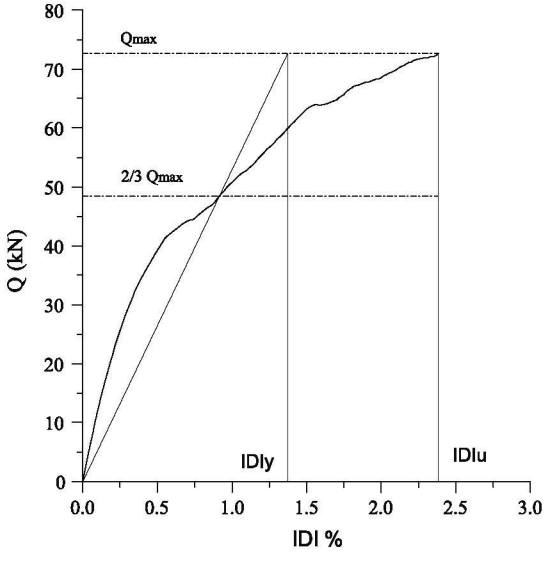

Fig. 15. Definition of yield and ultimate interstory drift index (IDI_y and IDI_u).

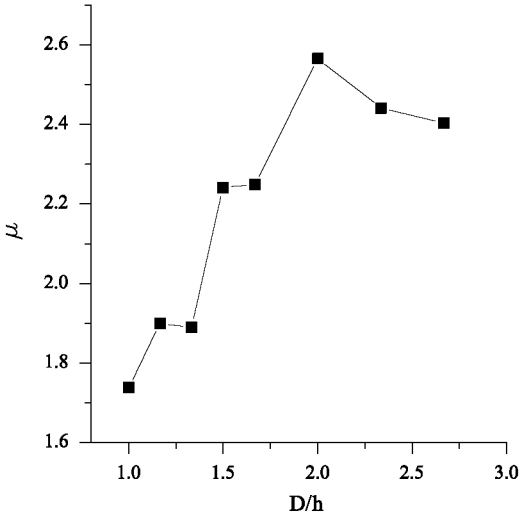

Fig. 16. Influence of the beam's depth normalized by the specimen model in the ductility of the connection.

increase of ductility in the range $(D/h) < 2$ is attributable to the reduction of stress concentration around the column face and the more uniform distribution of bending moment on the plate (see Fig. 14). Owing to these two factors, higher lateral displacements δ can be developed before the concrete attains its maximum compressive strain and makes the plate fail in flexure. From these results, it follows that increasing the depth of the beam beyond two times the thickness of the plate does not make any sense from the point of view of improving the ductility.

5.3. Influence of the depth of the transverse beam on effective width

The effective width b_{eff} of the WFP is defined here as the width of a virtual beam whose ultimate flexure capacity – assuming that all the steel located at the same distance from the neutral axis yields, coincides with the actual maximum bending moment that can be sustained by the WFP.

In the analysis of the numerical models under monotonic loading, the maximum lateral load capacity Q_u of the connection was attained when the WFP cross section located at one side of the column reached its ultimate flexure capacity under negative bending moments $M^-_{u,tot}$. The value of $M^-_{u,tot}$ was calculated for each numerical model (see Table 4), from which b_{eff} was estimated by solving in the following equation,

$$\left|M^-_{u,tot}\right| = A_{s,eff} f_s d \left[1 - \frac{A_{s,eff} f_s}{1.7 b_{eff} f'_c d}\right] \quad (3)$$

where $A_{s,eff}$ is the area of tension (top) reinforcement located within the width b_{eff}. Fig. 17 shows the b_{eff} obtained in this way for each numerical model characterized by the ratio D/h. In the vertical axis b_{eff} is normalized by the corresponding value in the model D18, $b_{eff,D18}$ ($1.31\ \text{m} \approx 6h + c_2$). Figure shows that up to $D/h = 1.5$ the effective width b_{eff} increases almost linearly with the depth of the transverse beam, but beyond $D/h = 1.5$ increasing the depth of the transverse beam does not improve the effective width of the WFP.

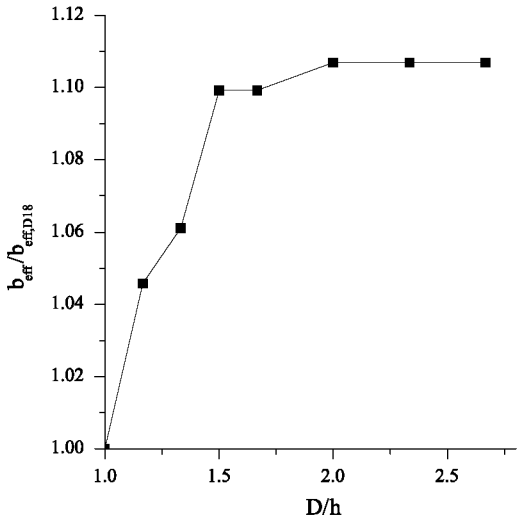

Fig. 17. Relationship between effective width of WFP and depth of the transverse beam.

6. Conclusions

A numerical study was conducted on interior waffle flat plate–column connections to investigate the share of the unbalanced moment caused by lateral loads between flexure and excentricity of shear, and the influence of the transverse beams. A non-linear finite element model (benchmark model) was built and calibrated with the results of quasi-static cyclic tests. From this benchmark, additional models were developed by varying the depth of the transverse beams. The following conclusions can be made:

(a) The portion of unbalanced moment transferred by the excentricity of shear about the centroid of the critical section defined by Eurodoce-2 according to the numerical results, is very close to the value (0.6) prescribed by this code.
(b) In contrast, the portion of unbalanced moment to be transferred by excentric shear according to ACI 318-11 is far below (42% less than) the actual value obtained from the numerical simulations. This leads to an unsafe shear design of the connection.
(c) The Section 13.5.3.3 of ACI 318-11 permits a reduction in γ_v from 0.40 up to 0.25 if two conditions related to the value of the gravity shear force and the amount of reinforcement are accomplished, as in this case. However, the results of this study show that such reduced values of γ_v are unsafe because γ_v can reach up to $\gamma_v = 0.69$. This conclusion has also been found in past studies [7,8,18]. Therefore, the authors recommend removing Section 13.5.3.3 from ACI 318-11 because it leads to unsafe structural designs on punching stress.
(d) The increase of the depth D of the transverse beam over the thickness of the plate h, flattens the bending moment distribution along the cross section of the plate and increases the ductility of the connection up to 50% for $D/h = 2$. Increasing D beyond $2h$ does not provide any additional improvement on the ductility.
(e) An effective width b_{eff} for the waffle flat plate based on the equivalence of flexural strength was defined. For transverse beams with the same depth as the plate, b_{eff} was found to be approximately the column width plus 6 times the thickness of the plate. Although b_{eff} can be increased up to about 10% by raising D, increasing D beyond $1.5h$ does not provide any additional increase of b_{eff}.

Acknowledgements

This research was funded by the local government of Spain, *Consejería de Innovación, Ciencia y Tecnología* (Project P07-TEP-02610)

and by the European Union (*Fonds Européen de Dévelopment Régional*).

References

[1] Ministerio Fomento. Norma de Construcción Sismorresistente: Parte general y edificación (NCSE-02), 2004 edn. Centro Publicaciones-Ministerio Fomento-España; 2003.
[2] European Committee for Standardisation. Eurocode 2: design of concrete structures. CEN; 2011.
[3] ACI Committee 318. Building code requirements for reinforced concrete (ACI 318M-11) and commentary. American Concrete Institute; 2011.
[4] Hanson NW, Hanson JM. Shear and moment transfer between concrete slabs and columns. Portland Cem Assoc 1968;10(29):2–16.
[5] Ritchie M, Ghali A, Dilger W, Gaye RB. Unbalanced moment resistance by shear in slab–column connections: experimental assessment. ACI Struct J 2006;1(103):74–82.
[6] Abdul-Wahab HMS, Khalil MH. Rigidity and strength or orthotropic reinforced concrete waffle slabs. J Struct Eng 2000;126(2):219–27.
[7] Mast PE. Stresses in flat plates near columns. ACI J Proc 1970;67(10):761–8.
[8] Elgabry A, Ghali A. Moment transfer by shear in slab–column connections. ACI Struct J 1996;93(2):187–96.
[9] Benavent-Climent A, Cahís X, Catalán A. Seismic behavior of interior connections in existing waffle–flat-plate structures. Eng Struct 2008;30(9):2510–6.
[10] Donaire-Avila J, Benavent-Climent A. Validación numérica del comportamiento cíclico de conexiones interiores en estructuras con forjados reticulares. Rev. Int. Met. Numer. 2012;28(4):256–67. http://dx.doi.org/10.1016/j.rimni.2012.08.003.
[11] Maekawa K, Pimanmas A, Okamura H. Nonlinear mechanics of reinforced concrete. Spon Press; 2003.
[12] Rashid YR. Analysis of prestressed concrete pressure vessels. Nucl Eng Des 1968;7:334–44.
[13] Polak MA. Reinforced concrete shell elements subjected to bending and membrane loads. Thesis/dissertation. University of Toronto, Toronto, Canada; 1992.
[14] Irawan P, Maekawa K. Path-dependent non-linear analysis of reinforced concrete shells. J Mater Concr Struct Pavements 1997;34:121–34.
[15] Ministerio Fomento. EHE-08. Instrucción de Hormigón Estructural, 2ª Edición edn. Centro Publicaciones-Ministerio Fomento; 2009.
[16] ACI Committee 318. Publication SP-10: commentary on building code requirements for reinforced concrete (ACI 318-62). ACI, Detroit, Michigan; 1965.
[17] Yamazaki J, Hawkins NM. Behavior of concrete plates joined to columns. Proc JSCE 1979;292:117–30.
[18] Gayed RB, Ghali A. Unbalanced moment resistance in slab–column joints: analytical assessment. J Struct Eng 2008;134(5):859–64.
[19] Forum8co, L. Engineer's Studio. Computer program, Tokyo, Japan; 2011 [1.6.03].
[20] Austin P, Moehle JP. Lateral displacement ductility of reinforced concrete flat plates. ACI Struct J 1989;86(3):250–8.